Supporting Information: Probing adsorption interactions of lignin derivatives in industrial zeolite catalysts through combining vibrational spectroscopy and *ab initio* calculations

K. S. C. Morton[a,b,c], A. J. O. Malley[a,b]*, J. Armstrong[c]*

[a]Institute for Sustainability, Department of Chemistry, University of Bath, BA2 7AY, UK
[b]UK Catalysis Hub, Research Complex at Harwell, Rutherford Appleton Laboratory, Didcot, Oxford, OX11 0FA, UK.
*Email: a.o'malley@bath.ac.uk
[c]ISIS Pulsed Neutron and Muon Facility, Rutherford Appleton Laboratory, Didcot, Oxford, OX11 0QX, UK.
*Email: jeff.armstrong@stfc.ac.uk

S1 Zeolite properties

Table S1: Textural properties of the experimentally applied zeolite frameworks HY, H-Beta and H-ZSM-5.

Zeolite	**BET Surface Area (mg^2g^{-1})**	**External Surface Area (mg^2g^{-1})**	**Internal Surface Area (mg^2g^{-1})**	**Mesopore Volume (cm^3g^{-1})**	**Micropore Volume (cm^3g^{-1})**
HY (CBV720)[1]	926	201	725	0.222	0.281
H-Beta (CP814E*)[2]	492	183	304	0.160	0.769
H-ZSM-5 (CBV2314)[3]	376	276	100	0.074	0.128

S2 Building the simulated zeolite frameworks

Table S2: The unit cell parameters of the zeolite frameworks HY, H-Beta and H-ZSM-5.

Zeolite Type	**a**	**b**	**c**	α	β	γ
HY	17.698	17.698	17.698	60.0	60.0	60.0
H-Beta	12.661	12.661	26.406	90.0	90.0	90.0
H-ZSM-5	19.879	20.107	13.369	90.0	90.7	90.0

S3 Preliminary calculations

S3.1 Testing convergence criteria

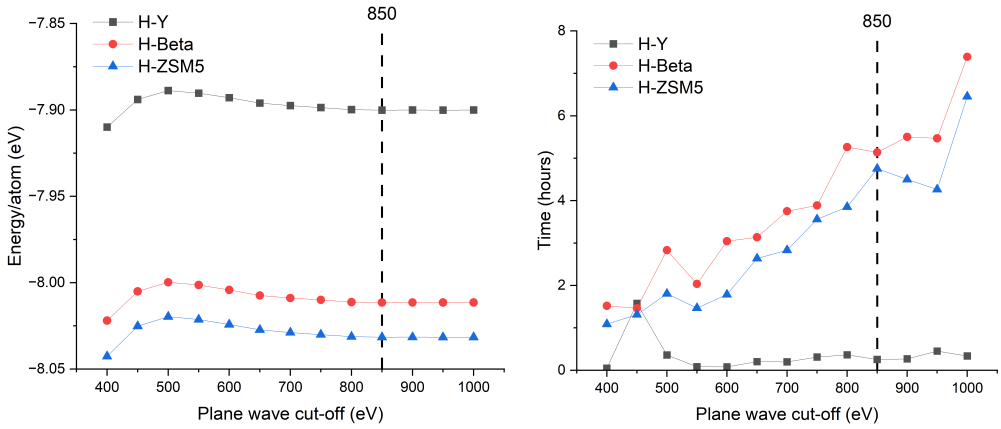

(a) (b)

Figure S1: (a) The energy per atom for each zeolite framework varying with plane wave cutoff energy and (b) the computational expense for each calculation.

S3.2 Brønsted acid site placement

A comparison of the experimental inelastic neutron scattering (INS) spectrum and simulated spectrum of zeolite H-Y with the acidic proton placed at O4 are shown in Figure S2.

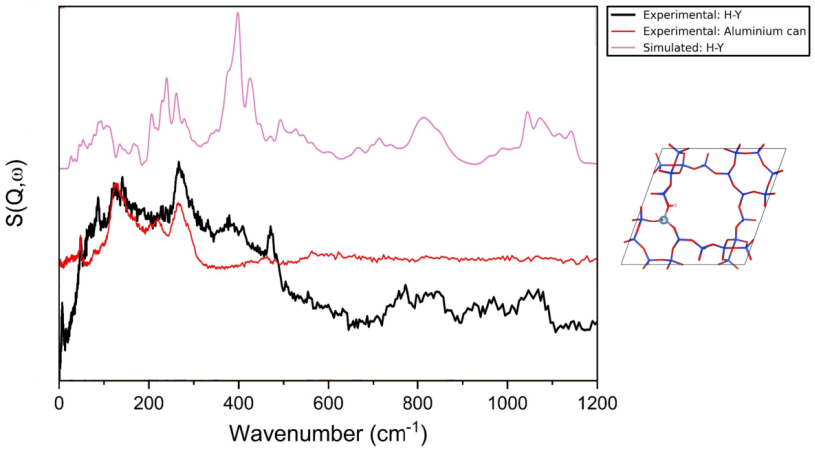

Figure S2: Simulated spectrum of H-Y compared to the experimental INS spectrum.

The experimental and simulated spectra of zeolite H-Beta with one or two Brønsted acid site (BASs) placed in the most probable positions according to numerous studies[4–9] are compared in Figure S3, showing good agreement for the T1O4 model and potentially the T2O7 model. While it is possible that both sites

may well be present, recent studies have suggested that T1 is more favourable for single Al substitution[4]. The oxygen atoms were placed as per their lowest energy position according to Li *et al.*[4].

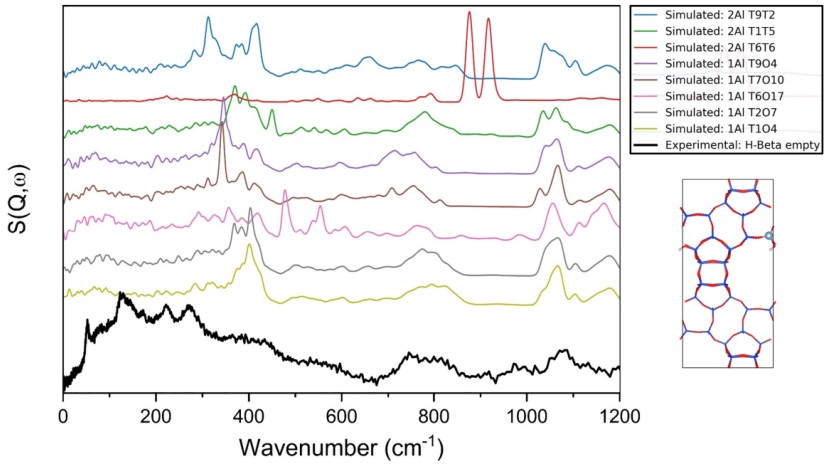

Figure S3: Simulated spectra of H-Beta with varying acid site locations (different T-sites) and numbers compared to the experimental INS spectrum of empty H-Beta.

The experimental and simulated spectra of zeolite H-ZSM5 with BASs placed in the most probable positions according to numerous studies[10,11] are compared in Figure S4, showing good agreement for the monoclinic T1 model. Orthorhombic H-ZSM5 structures were also compared, formed above 340 K, with many studies investigating favourable BAS placement within this structure[12–19].

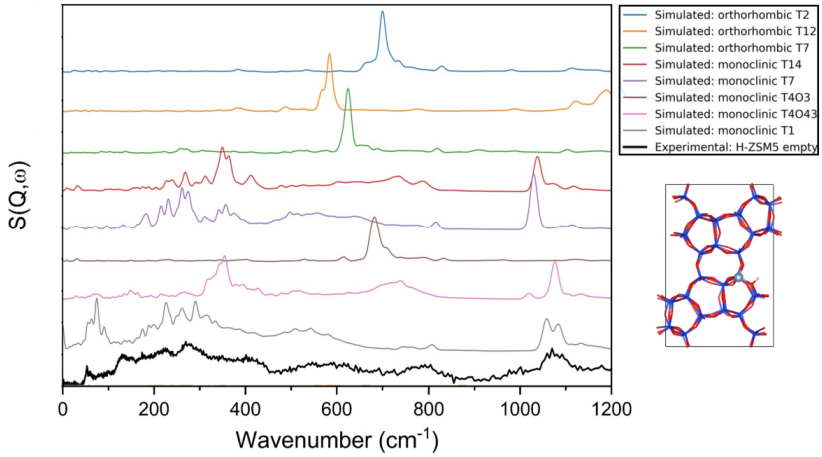

Figure S4: Simulated INS spectra of H-ZSM5 with varying acidic site locations (different T-sites) compared to the experimental INS spectrum of empty H-ZSM5.

In each INS spectrum of the empty zeolite samples similar modes featuring at similar wavenumbers are exhibited. The sharper peaks observed at approximately 75, 150, 240 and 290 cm^{-1} largely come from the aluminium of the sample container. However, other features from the zeolite framework contribute to the region below 500 cm^{-1} relating to framework vibrations. The broad adsorption bands in this region have been observed previously in zeolite Y and ZSM5 due to lattice modes from anti-symmetric

T-O vibrations[20]. The features at approximately 400 and 1100 cm^{-1} have previously been identified as an out-of-plane and two in-plane SiOH bending modes respectively, which are also in agreement with our simulated spectra[21,22]. The broad peak around 800 cm^{-1} has previously been recognised as the first overtone of the out-of-plane SiOH bending[22]. Our simulations agree, but additional symmetric and asymmetric stretching T-O modes also add to this peak at around 770 cm^{-1}, corroborated by Jacobs*et al.*[21]. The aforementioned modes have also been documented in other zeolites through INS, infra-red spectroscopy and *ab initio* techniques[23,24].

S3.3 Increasing the cresol loading

The experimental systems had high acid site densities (Si/Al from 11.5-15.0) and loadings (10% wt.) to better represent catalytic systems and to get a significant proportion of hydrogen into the neutron beam to increase scattering. Based on the zeolite unit cell structures, this corresponds to 2-3, 3-4 and 5-6 cresol molecules loaded into H-Y, H-Beta and H-ZSM5 respectively. Hence, we tested our DFT systems to see how much the impact of increasing the loading of cresol molecules had on its ability to reproduce experimental INS spectra. Shown in Figure S5 are simulated spectra of zeolite H-Y systems loaded with 1-3 *p*-cresol molecules to observe the effect of increased loading to the vibrational spectra produced. Different loadings of *p*-cresol were added into systems containing 1 or 3 acid sites to observe the effect to the spectra when all molecules are bonded to acid sites, or all molecules are non-bonded, and when mixtures of both bonded and non-bonded cresols are present. It is important to note that in each experimental sample there are more acid sites compared to cresol molecules, meaning that it was possible for every molecule to bond to an acid site. In H-Y, H-Beta and H-ZSM5 there are 1.13, 1.33 and 1.45 acid sites available per cresol/anisole molecule and 1.30, 1.53 and 1.66 acid sites per guaiacol respectively.

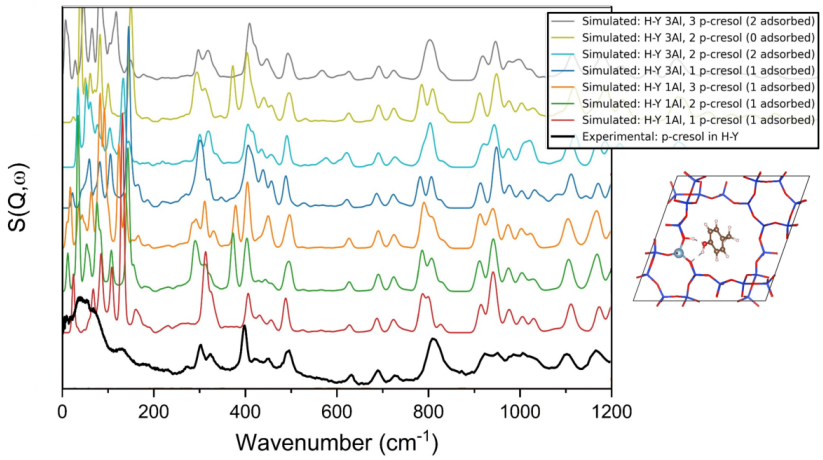

Figure S5: Simulated spectra of H-Y with 1-3 molecules of *p*-cresol adsorbed to 1-3 BASs (1Al or 3Al), compared to the experimental INS spectrum.

Each model gave a fairly good match to the experiment. The models containing molecules of *p*-cresol that were not adsorbed to a BAS (and also not bonded to another *p*-cresol molecule) all contained an

extra peak at ∼390 cm^{-1}. This corresponds to an OH out-of-plane mode that was not observed in the experimental INS spectrum. The only spectra containing an unbound *p*-cresol molecule without this OH bend was the model containing cresols at a 2:1 bonded to non-bonded ratio. This is thought to be because at a loading of 3 molecules per unit cell (higher than that of the experiment) this mode is also restricted in the non-bonded cresol due to spatial limitations. Therefore, at a loading of 10% wt., it is possible that some cresol molecules are non-bonded to acid sites but show similar vibrations to those that do bond to acid sites. However, cresols adsorbed to the BASs in the 3Al systems exhibited an extra peak at ∼600 due to a vibration of the BAS proton pointing into the 12 MR of the sodalite cage, which was not present in the experimental spectrum.

In the experimental samples, it is possible that in systems of this magnitude and with a high loading of sorbates, the cresol molecules are present in numerous positions, both bonded and non-bonded to BASs, which are likely to be heterogeneously distributed throughout the zeolite structure. However, the good match of the simulated spectrum calculated from models involving only a single BAS bonded to a single adsorbate to the experimental spectrum, suggests that this structure commonly occurs within the experiment. This also agrees with the works of Sivasankar *et al.* who observed that benzene - expected to bind less strongly than the lignin derivatives investigated here - adsorbed favourably to the zeolite BASs, only adsorbing to non-BAS locations as the loading increased as all accessible BAS spots were filled[25]. The work indicated that adsorbate clustering or other intermolecular interactions were not significant in either the acidic or silicate forms of the zeolite. Therefore, to simplify the results, the single BAS-single adsorbate model was applied to further simulations.

S3.4 Functional choice

The choice of functional is often important for obtaining accurate adsorption energies. However, for the purpose of this study it was more important to gather information on adsorption energy trends with the type of zeolite and adsorbed monomer. Different functionals were trialled in their ability to recreate the experimental INS spectra, shown in Figure S6, based on their previous applications in the literature. Such functionals included PBE with a D2 dispersion correction[26,27], or D3 dispersion correction[28–30], PBEsol for zeolite parameter optimisation[31], PW91 and B3LYP[32]. A study comparing 10 different DFT functionals and a hybrid functional found that the adsorption of water molecules to zeolite SSZ-13 gave structurally similar results. PBE-D3 was found to reproduce the same trends as the more accurate post Hartree-Fock methods (RPA and MP2) and this was consistent across different adsorption sites, but it did overestimate the binding energy[33], whereas revPBE was accurate to within 5 $kJmol^{-1}$[34]. Plessow *et al.* also found that whilst PBE-D3 overestimated the binding energies by around 50 $kJmol^{-1}$, the change in energy with different zeolite catalysts is much more accurate, to within 5 $kJmol^{-1}$, making it a suitable functional for studying such trends[28].

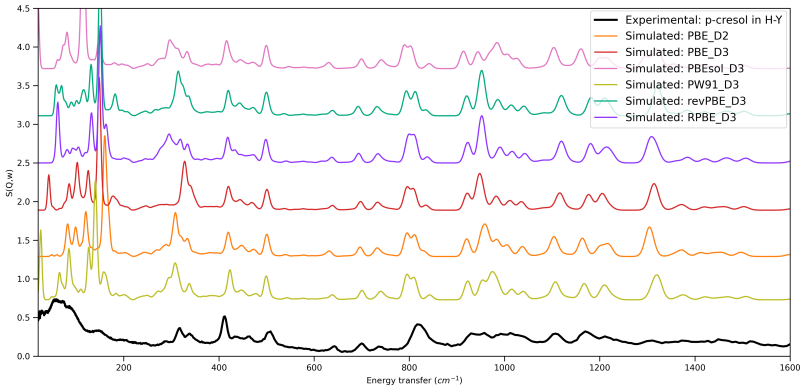

(a)

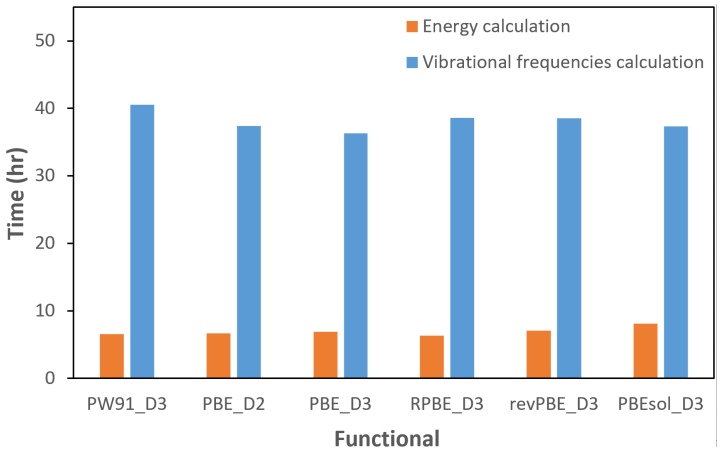

(b)

Figure S6: (a) Simulated INS spectra applying different functionals compared to the experimental INS spectrum of *p*-cresol in H-Y and (b) the time taken for each calculation.

Seen in Figure S6(a), the optimisation and phonon calculation produced applying each functional gives an adequate match to the INS spectrum. This suggests that the choice of functional does not greatly affect the vibrational spectra produced. In Figure S6(b), each of the GGA functionals were similarly expensive, except B3LYP which was over six times more expensive compared to every other functional tested and hence not included here. Following on from this, the PBE functional with D3 dispersion correction was chosen for all sequential studies due to its vast application in the literature, ability to reproduce accurate trends in adsorption energies with zeolite type and adsorbate, and its low computational cost.

S4 Adsorption conformations and energies

The final, lowest energy adsorption conformations for each monomer in each framework are shown in Figures S7-S9.

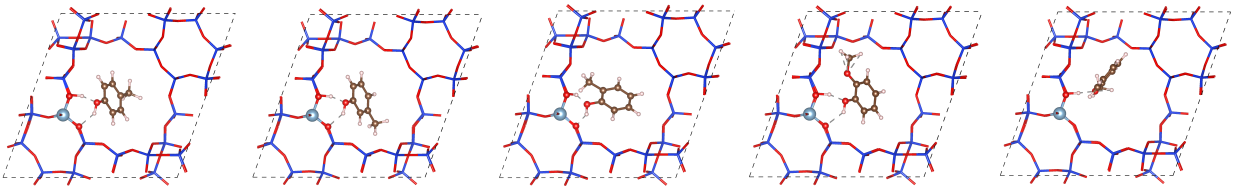

(a) *p*-Cresol (b) *m*-Cresol (c) *o*-Cresol (d) Guaiacol (e) Anisole

Figure S7: Adsorption conformations of lignin derivatives in H-Y.

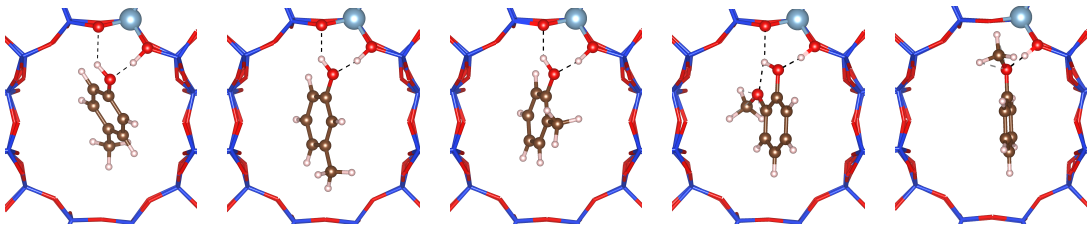

(a) *p*-Cresol (b) *m*-Cresol (c) *o*-Cresol (d) Guaiacol (e) Anisole

Figure S8: Adsorption conformations of lignin derivatives in H-Beta.

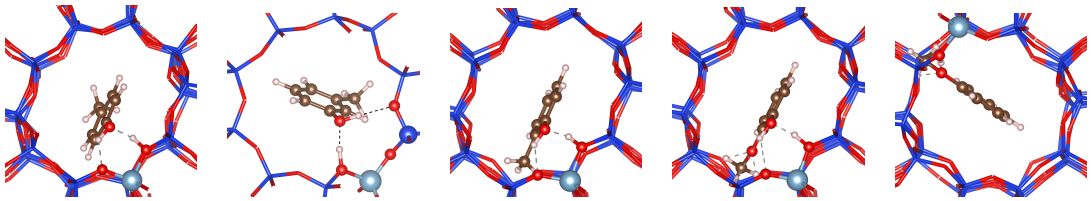

(a) *p*-Cresol (b) *m*-Cresol (c) *o*-Cresol (d) Guaiacol (e) Anisole

Figure S9: Adsorption conformations of lignin derivatives in H-ZSM5.

The adsorption energies (E_{ads}) were calculated applying equation 1 using the final energies of the empty zeolite ($E_{zeolite}$), single adsorbate molecule ($E_{adsorbate}$) and an adsorbate bonded within a zeolite ($E_{adsorbate+zeolite}$).

$$E_{ads} = E_{adsorbate+zeolite} - (E_{adsorbate} + E_{zeolite}) \tag{1}$$

The trends in adsorption energy with zeolite and adsorbate type are listed in Table S3, alongside the associated BAS-to-adsorbate H-bonding lengths (H_{BAS}-to-O_{ads}) and angles (O_{BAS}-to-H_{BAS}-to-O_{ads}). When the adsorbate conformation formed a 5-membered ring (MR) or 8-MR ring structure the lengths (H_{ads}-to-O_{zeo}) and angles (O_{ads}-to-H_{ads}-to-O_{zeo}) of the additional bonds formed are also given, as well as the intramolecular bond lengths (H_{ads}-to-O_{ads}) and angles (O_{ads}-to-H_{ads}-to-O_{ads}) formed in guaiacol.

Figure S10 and Figure S11 show variations in bond lengths and angles respectively for both H-bonds formed with zeolite and adsorbate type.

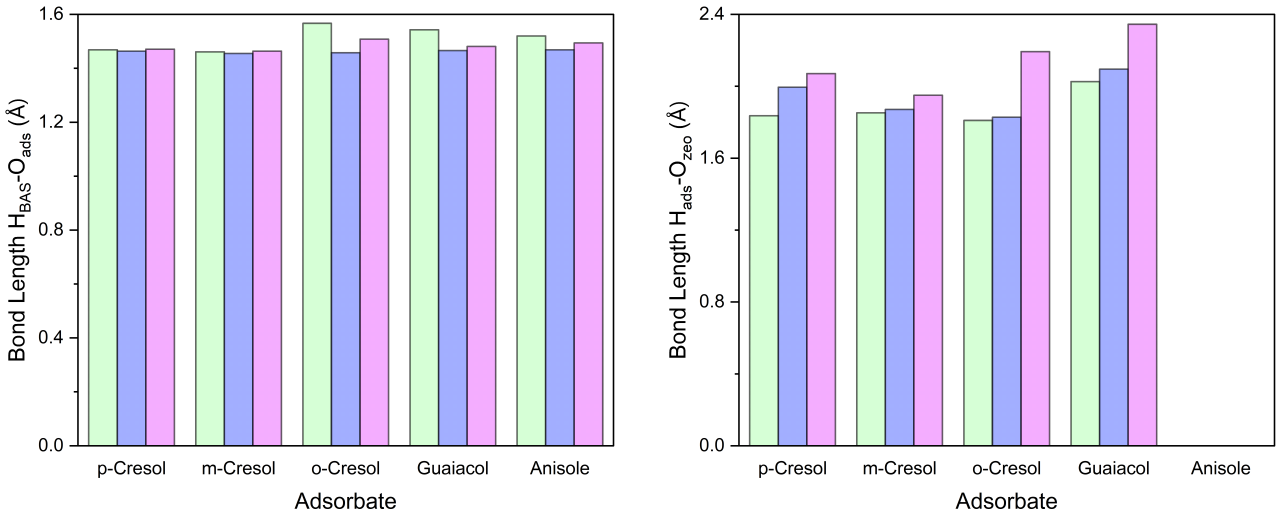

(a) H_{BAS}-to-O_{ads} (b) H_{ads}-to-O_{zeo}

Figure S10: The bond lengths between different lignin derivatives and zeolites H-Y (green), H-Beta (blue), and H-ZSM5 (purple).

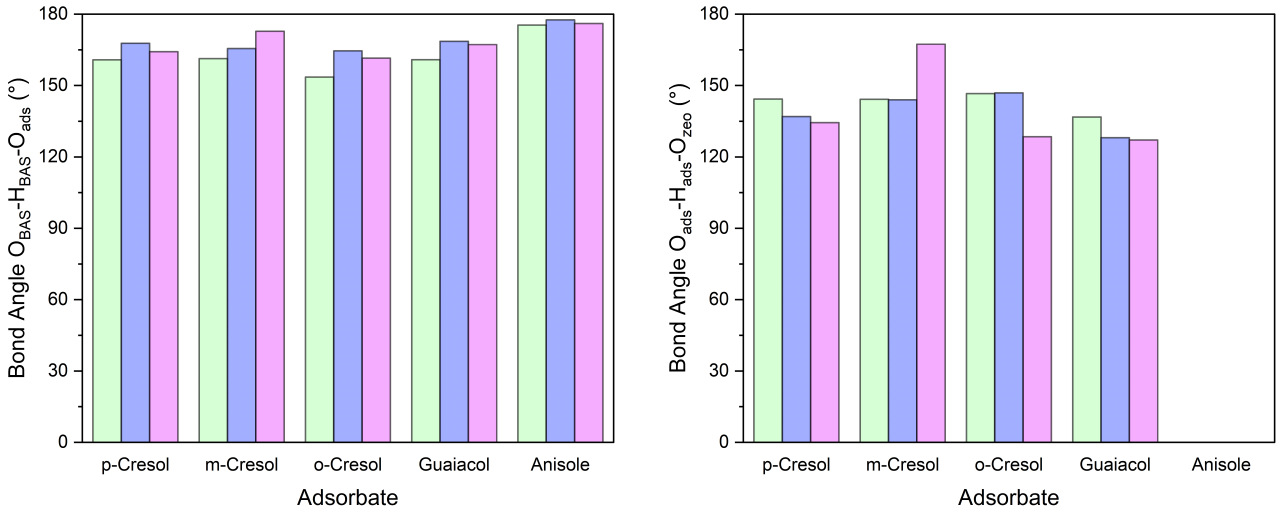

(a) O_{BAS}-to-H_{BAS}-to-O_{ads} (b) O_{ads}-to-H_{ads}-to-O_{ads}

Figure S11: The bond angles between different lignin derivatives and zeolites H-Y (green), H-Beta (blue), and H-ZSM5 (purple).

Table S3: The bond angles, bond lengths and adsorption energies calculated for lignin derivatives in zeolite H-Y, H-Beta and H-ZSM5.

Zeolite	Adsorbate	Bond Type	Bond Angle (°)	Bond Distance (Å)	Adsorption Energy (kJ mol^{-1})
H-Y	*p*-Cresol	O_{BAS}-H_{BAS}—O_{ads}	160.8	1.469	-117.7
		O_{ads}-H_{ads}—O_{zeo}	144.3	1.836	
	m-Cresol	O_{BAS}-H_{BAS}—O_{ads}	161.3	1.461	-114.1
		O_{ads}-H_{ads}—O_{zeo}	144.2	1.852	
	o-Cresol	O_{BAS}-H_{BAS}—O_{ads}	153.6	1.577	-109.7
		O_{ads}-H_{ads}—O_{zeo}	146.6	1.810	
	Guaiacol	O_{BAS}-H_{BAS}—O_{ads}	160.9	1.543	-104.5
		O_{ads}-H_{ads}—O_{zeo}	136.8	2.026	
	Anisole	O_{BAS}-H_{BAS}—O_{ads}	175.4	1.520	-97.4
H-Beta	*p*-Cresol	O_{BAS}-H_{BAS}—O_{ads}	167.8	1.464	-137.6
		O_{ads}-H_{ads}—O_{zeo}	137.0	1.995	
	m-Cresol	O_{BAS}-H_{BAS}—O_{ads}	165.54	1.455	-137.6
		O_{ads}-H_{ads}—O_{zeo}	144.0	1.871	
	o-Cresol	O_{BAS}-H_{BAS}—O_{ads}	164.6	1.458	-133.3
		O_{ads}-H_{ads}—O_{zeo}	146.9	1.828	
	Guaiacol	O_{BAS}-H_{BAS}—O_{ads}	168.6	1.466	-136.1
		O_{ads}-H_{ads}—O_{zeo}	128.1	2.095	
		O_{ads}-H_{ads}—O_{ads}	103.6	2.251	
	Anisole	O_{BAS}-H_{BAS}—O_{ads}	177.6	1.469	-128.4
H-ZSM5	*p*-Cresol	O_{BAS}-H_{BAS}—O_{ads}	164.2	1.471	-152.1
		O_{ads}-H_{ads}—O_{zeo}	134.4	2.071	
	m-Cresol	O_{BAS}-H_{BAS}—O_{ads}	172.8	1.464	-142.4
		O_{ads}-H_{ads}—O_{zeo}	167.4	1.950	
	o-Cresol	O_{BAS}-H_{BAS}—O_{ads}	160.8	1.493	-144.7
		O_{ads}-H_{ads}—O_{zeo}	128.5	2.118	
	Guaiacol	O_{BAS}-H_{BAS}—O_{ads}	167.2	1.481	-156.7
		O_{ads}-H_{ads}—O_{zeo}	124.1	2.345	
		O_{ads}-H_{ads}—O_{ads}	113.2	2.066	
	Anisole	O_{BAS}-H_{BAS}—O_{ads}	176.1	1.494	-133.1

S5 Inelastic Neutron Scattering

S5.1 Vibrational modes of lignin derivatives

As all INS measurements are taken below 10 K, the lignin derivative samples form pure compounds, meaning intermolecular adsorbate-adsorbate interactions will be present such as H-bonding. It is hard to predict exactly how crystals form between molecules with such a rapid reduction in temperature and with few experimental crystal structures available for the aforementioned samples, obtained through single-crystal X-ray techniques. It is also likely that polymorphism, the ability of a compound to crystallise in different forms, is apparent in these samples. For example, crystal structures all obtained from single crystal X-ray experiments saw monoclinic crystalline *p*-cresol with $P2_1/n$ and C2/c space groups at 173 K crystallised from different solvent solutions[35] and $p2_1/c$ at 123 K[36]. Another study also observed C2/c space groups at room temperature[37].

Vibrational frequencies were obtained from the most suitable crystal structures available[38]. We also compared the crystal structure calculation to single molecule calculations, by placing single molecules in a box of sufficient size to inhibit periodic images interacting. The simulated spectra obtained were compared to the experimental INS spectra, enabling the identification of the dynamic modes corresponding to each peak. The shaded regions in each spectrum represent calculated overtones.

First, we show the experimental and simulated vibrational spectra of *p*-cresol shown in Figure S12, with the crystal structure obtained by Bois at 123 K[36] used as the initial model for the simulations.

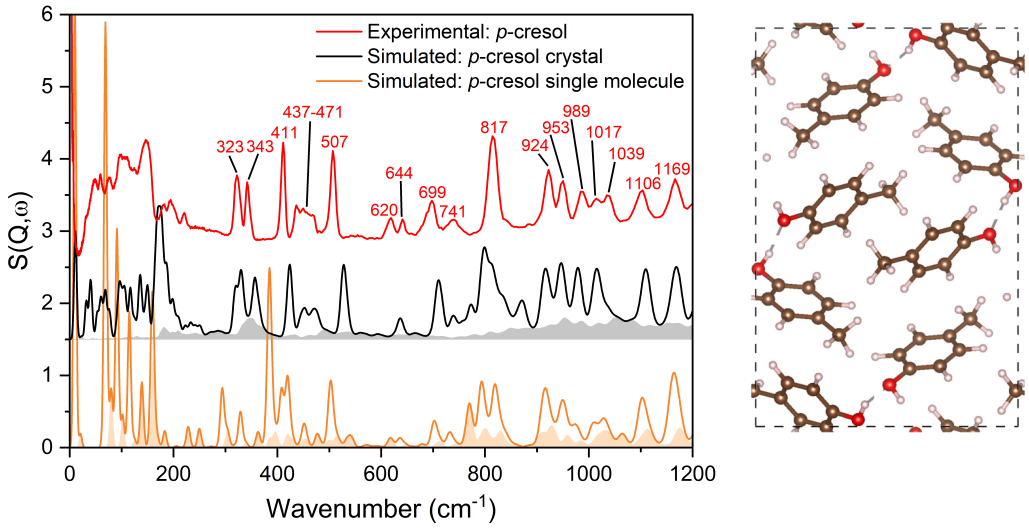

(a) (b)

Figure S12: (a) Experimental INS spectrum of crystalline *p*-cresol compared against the simulated spectra of a single molecule and crystalline *p*-cresol, with the structure shown in (b).

For *m*-cresol there was only one crystalline structure available with $P2_1/c$ symmetry published by Bois *et al.* and measured at 173 K[39].

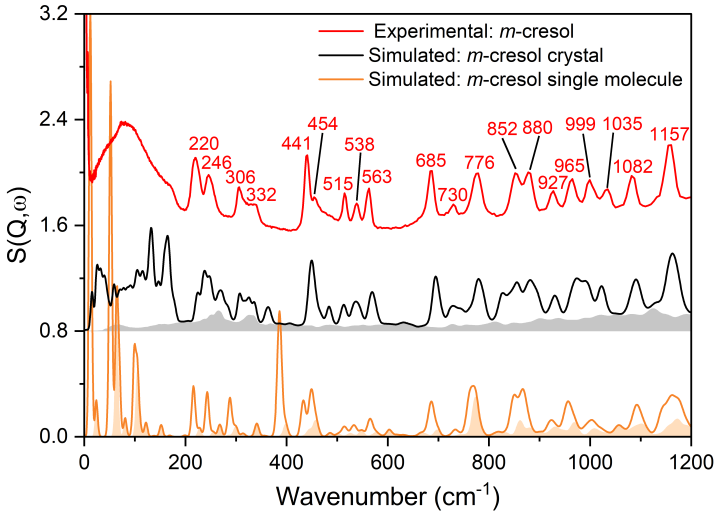

(a)

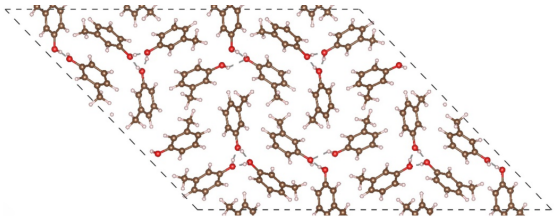

(b)

Figure S13: (a) Experimental INS spectrum of crystalline *m*-cresol compared against the simulated spectra of a single molecule and crystalline *m*-cresol, with the structure shown in (b).

For *o*-cresol structures with $P3_2$ symmetry at 100 K with 3 molecules per asymmetric unit[40] and $P3_1$ symmetry at 223 K[41] were available. The structure taken at the lower temperature gave a better match to the simulated system, shown in Figure S14.

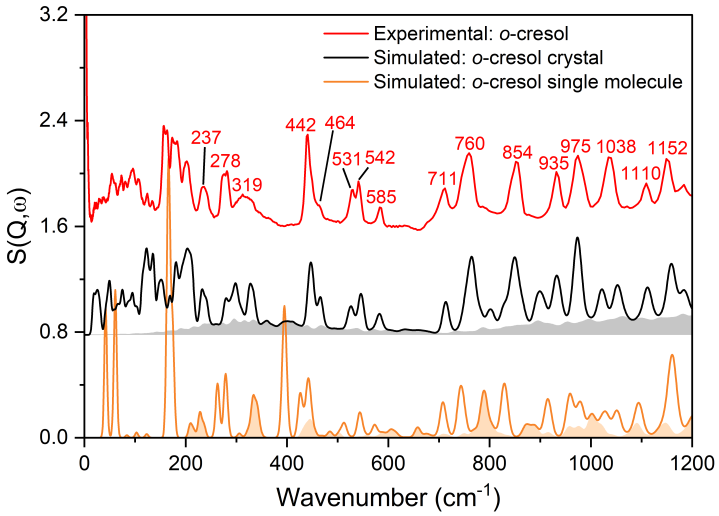

(a)

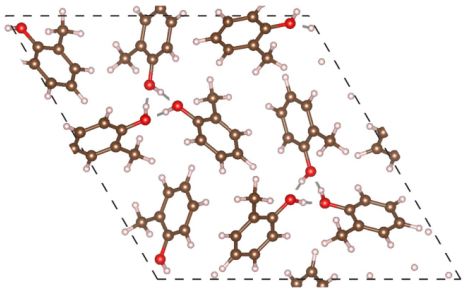

(b)

Figure S14: (a) Experimental INS spectrum of crystalline *o*-cresol compared against the simulated spectra of a single molecule and crystalline *o*-cresol, with the structure shown in (b).

The crystal structure applied for anisole had a $P2_1/c$ space group at 100 K[42], shown in Figure S15 (b), with the associated vibrational spectrum is shown in Figure S15 (a).

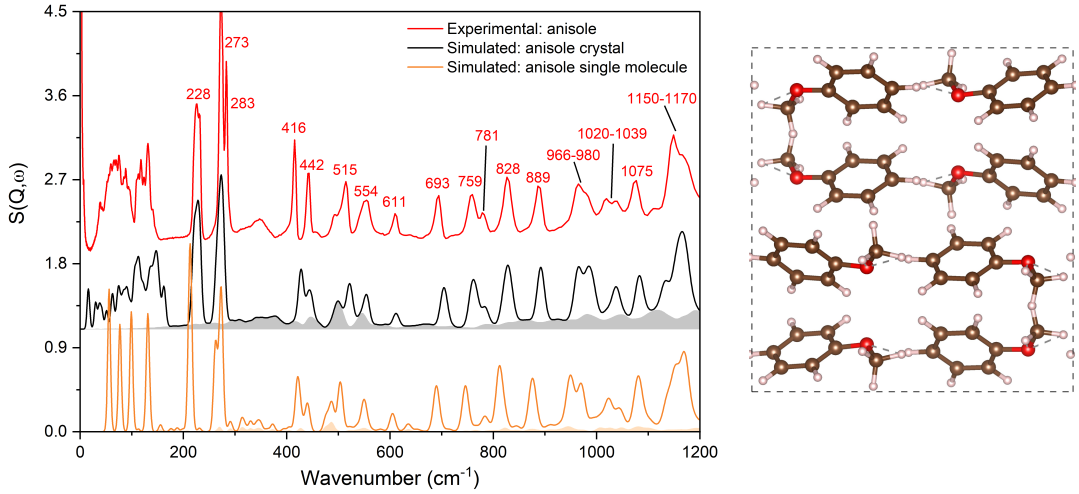

(a) (b)

Figure S15: (a) Experimental INS spectrum of crystalline anisole compared against the simulated spectra of a single molecule and crystalline anisole.

Unfortunately, no crystal structure was available for guaiacol, using the ConQuest Software[38]. Hence, the INS spectrum obtained from a sample of crystalline guaiacol was compared to the spectrum obtained from a calculation performed on a single molecule of guaiacol, shown in Figure S16. However, guaiacol has been measured using INS before, giving us confidence in the peak assignment discussed in Section **??**[43].

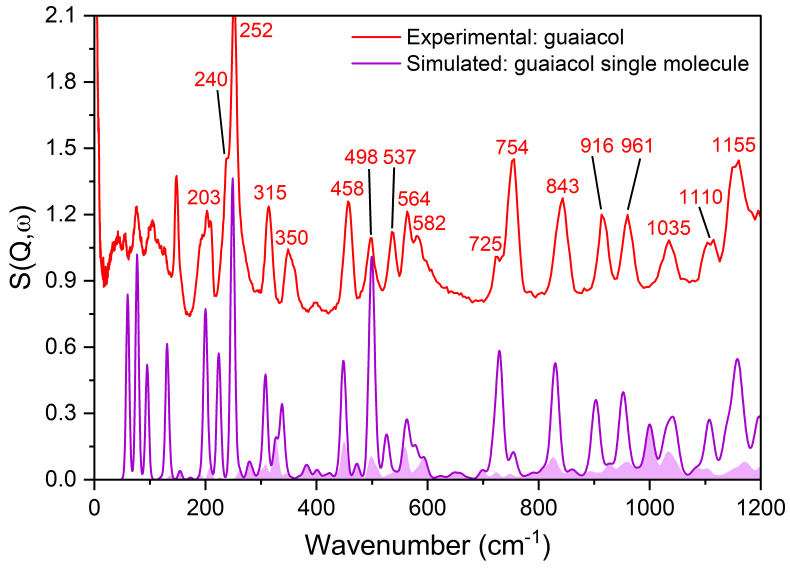

Figure S16: Experimental INS spectrum of crystal guaiacol compared against the simulated spectrum of a single molecule of guaiacol.

In all of the systems examined, the single-molecule spectra describe the experimental spectra to a large degree, enabling the identification of most of the modes associated with each peak. Spectra obtained from the calculated crystal systems exhibit advantages in capturing lower frequency modes, but assigning peaks at very low frequencies remains challenging. Comparative analysis reveals systematic downward shifts in wavenumbers unique to the single molecule calculations, absent in the crystal calculations. Additionally, distinct spectral peaks corresponding to hydroxy bends, less prevalent in both simulated and experimental crystalline spectra, are evident in the single molecule spectra, further highlighting the advantages of modelling the crystal system.

S5.2 Vibrational modes of derivatives in zeolites

In this section, we present comparisons between the vibrational INS spectra of each lignin monomer loaded into different zeolites and the corresponding simulated spectra. These analyses, in conjunction with the spectra observed in Section S3.1, were used to assign the majority of significant vibrational modes (involving hydrogen atoms) of the samples for each monomer from ∼150-1200 cm^{-1} shown in Tables S2-S6. The in-plane and out-of-plane modes are denoted ip and oop, with illustrations of the ip stretches and bending motions of the molecules shown in Figure S17(a), alongside the oop bends in Figure S17(b). Symmetric and asymmetric modes are designated sym and asym respectively.

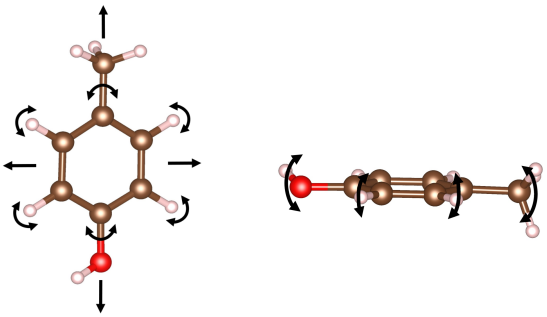

(a) ip bends and stretches

(b) oop bends

Figure S17: In-plane and out-of-plane *p*-Cresol vibrations.

Additionally, vibrational modes associated with specific functional groups are labelled as OH (hydroxyl), me (methyl), O (methoxy oxygen), Ome (methoxy), or ring (ring atoms). A ',' separates different functional groups and an 'and' separates different modes contributing to the same peak. Peaks beyond a certain wavenumber (approximately >1200 cm^{-1}) often exhibited insufficient resolution for assignment and so are omitted here, primarily comprising of hydrogen ip bends, ring stretching, methyl deformation modes and hydrogen stretching modes[44]. Any changes observed in the peaks associated with the monomer vibrational modes upon loading into zeolites are highlighted in column 3 of each respective table.

S5.2.1 *p*-Cresol

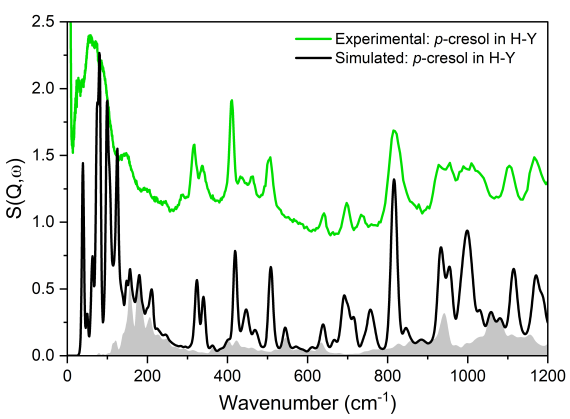

(a) *p*-Cresol in H-Y

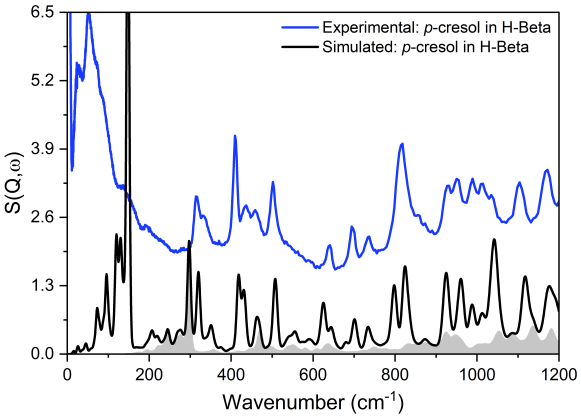

(b) *p*-Cresol in H-Beta

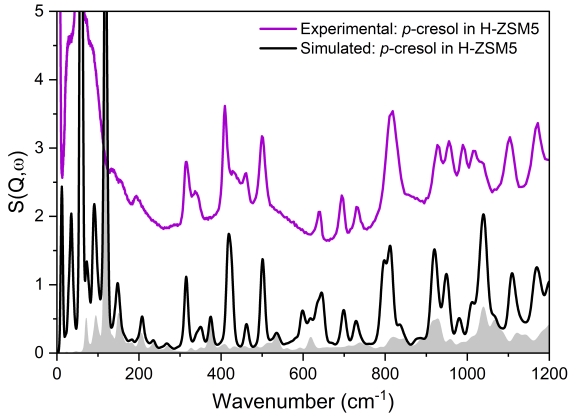

(c) *p*-Cresol in H-ZSM5

Figure S18: Comparisons of the simulated and experimental INS spectra used to identify modes related to each peak for *p*-cresol in each zeolite.

Table S4: Assignment of vibrational modes to peaks in the INS spectra of crystalline *p*-cresol and descriptions of the spectral changes upon its loading into zeolites.

Frequency (cm^{-1})	Vibrational modes	Significant spectral changes for the zeolite samples
323	sym me, OH ip bend	red-shift
343	OH, ring oop bend	reduced intensity, red-shift
411	asym ring oop bend	–
437-471	OH, ring ip bend, sym OH, me ip stretch	resolves into two peaks, red-shift
507	sym ring oop bend	reduced intensity, broadens
620	–	no peak
644	ring ip bend	–
699	ring oop bend	–
741	asym OH, me stretch	–
817	ring oop bend	broadens
924	ring oop bend	broadens, unresolved peaks from 953-1106
953	ring oop bend	see above
989	me ip bend	see above
1017-1039	ring ip bend and me oop bend	see above
1106	ring ip bend	–
1169	ring ip bend	–

S5.2.2 *m*-Cresol

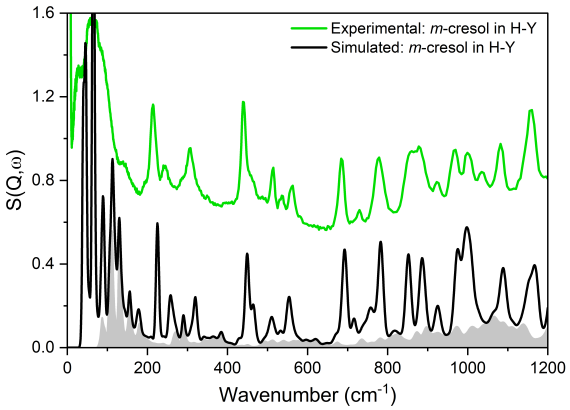

(a) *m*-Cresol in H-Y

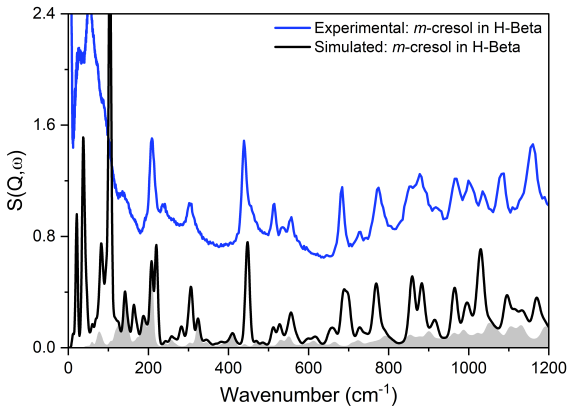

(b) *m*-Cresol in H-Beta

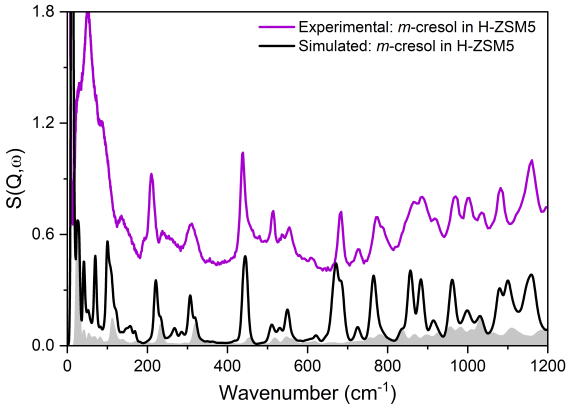

(c) *m*-Cresol in H-ZSM5

Figure S19: Comparisons of the simulated and experimental INS spectra used to identify modes related to each peak for *m*-cresol in each zeolite.

Table S5: Assignment of vibrational modes to peaks in the INS spectra of crystalline *m*-cresol and descriptions of the spectral changes upon its loading into zeolites.

Frequency (cm^{-1})	Vibrational modes	Significant spectral changes for the zeolite samples
220	sym me, OH oop bend	more defined, red-shift
246	OH, ring oop bend	reduced intensity, broader, red-shift
306-332	sym me, OH ip bends	unresolved peaks from 306-332
441	asym ring oop bend	–
515	asym all ip stretch	–
538	sym all ip stretch	reduced intensity
563	asym all oop bend	reduced intensity, red-shift
686	ring oop bend	–
730	sym all ip stretch	–
776	ring oop bend	broadens
852	ring oop bend	unresolved peaks from 852-927
880	ring oop bend	see above
927	all ip stretch	see above
965	ring oop bend	–
999	me, ring ip bend	–
1035	me oop bend	–
1082	ring ip stretch	–
1157	asym all stretch	–

As with *p*-cresol, when *m*-cresol is dosed into zeolites we observe many peak shifts to lower frequencies, especially for modes involving the hydroxyl group, alongside peaks that showed significant reductions in peak intensities, and peak broadenings, with greater changes observed going from H-Y to H-Beta to H-ZSM5. However, due to greater uncertainties in the peak assignments caused by unresolved peaks in the experiment and an insufficient reproduction of the experimental crystalline *m*-cresol spectrum, we have not investigated these changes in detail, as with other systems in Section 3.2.

S5.2.3 *o*-Cresol

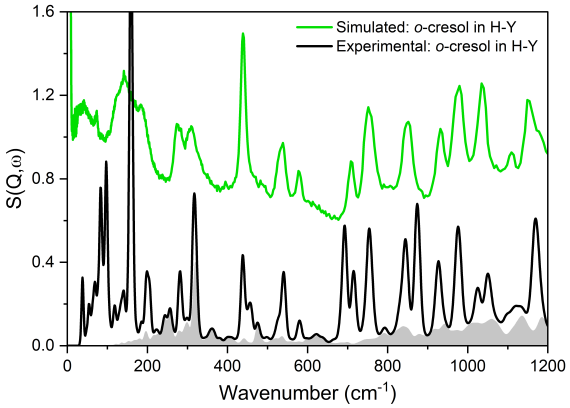

(a) *o*-Cresol in H-Y

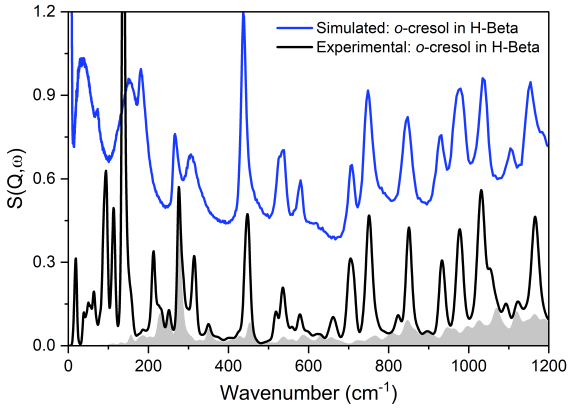

(b) *o*-Cresol in H-Beta

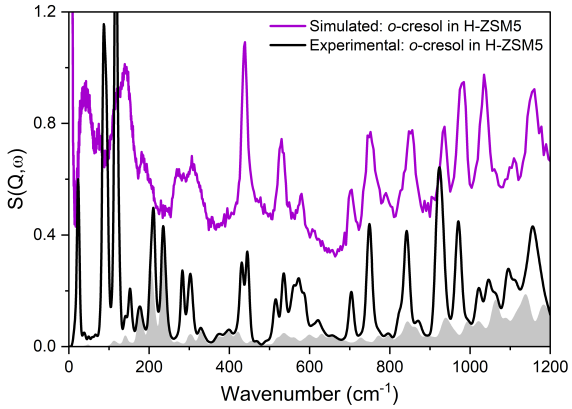

(c) *o*-Cresol in H-ZSM5

Figure S20: Comparisons of the simulated and experimental INS spectra used to identify modes related to each peak for *o*-cresol in each zeolite.

Table S6: Assignment of vibrational modes to peaks in the INS spectra of crystalline *o*-cresol and descriptions of the spectral changes upon its loading into zeolites.

Frequency (cm^{-1})	Vibrational modes	Significant spectral changes for the zeolite samples
278	sym all oop bend	decreased intensity, red-shift
319	sym OH me ip bend	red-shift
442	ring oop bend and OH ip bend	–
531–542	all ip bend and ip ring bend	unresolved peaks
585	all ip bend	red-shift
711	ring oop bend	red-shift
760	ring oop bend	red-shift
854	ring oop bend	broadens
935	ring oop bend	–
975	ring oop bend and me ip bend	–
1038	me oop bend and ring ip bend	decreased intensity
1110	ring ip bend	broadens
1152	ring ip bend	–

As with the other cresol molecules, when *o*-cresol is dosed into zeolites we observe many peaks that shift to lower frequencies, broaden and show significant reductions in peak intensities, with generally greater changes observed going from H-Y to H-Beta to H-ZSM5. However, as with *m*-cresol, there are greater uncertainties in the peak assignments.

S5.2.4 Anisole

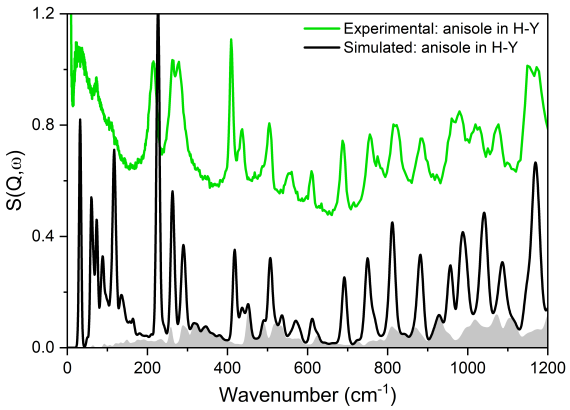

(a) Anisole in H-Y

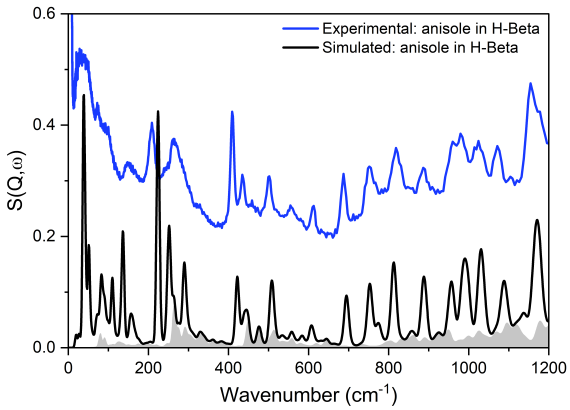

(b) Anisole in H-Beta

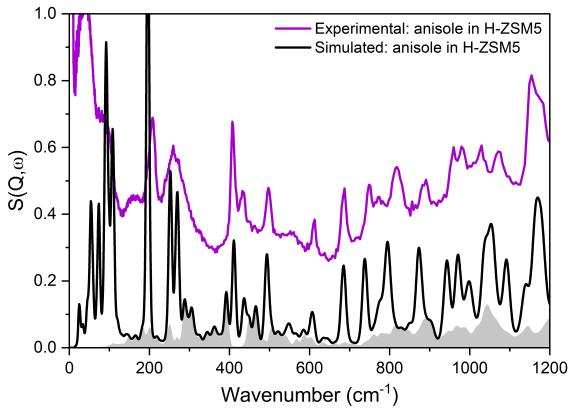

(c) Anisole in H-ZSM5

Figure S21: Comparisons of the simulated and experimental INS spectra used to identify modes related to each peak for anisole in each zeolite.

Table S7: Assignment of vibrational modes to peaks in the INS spectra of crystalline anisole and descriptions of the spectral changes upon its loading into zeolites.

Frequency (cm^{-1})	Vibrational modes	Significant spectral changes for the zeolite samples
225-239	me rotation, O oop bend and ring oop bend	decreased intensity, broadens, red-shift
273-283	me ip bend and me rotate, O, ring oop bend	decreased intensity, broadens and becomes less resolved, red-shift
416	ring oop bend	red-shift
442	all ip bend	decreased intensity, red-shift
515	ring, O oop bend	decrease intensity, left shoulder disappears
554	O oop bend	decreased intensity
611	ring ip bend	–
693	ring oop bend	red-shift
759	ring oop bend	red-shift
781	all ip stretch	decreased intensity
828	ring oop bend	broadens, red-shift
889	ring oop bend	broadens, decreased intensity
966-980	ring oop bend and ring ip stretch	–
1020-1039	all ip stretch	–
1075	ring ip stretch	reduced intensity
1150-1170	ring ip bend and Ome oop bend	–

S5.2.5 Guaiacol

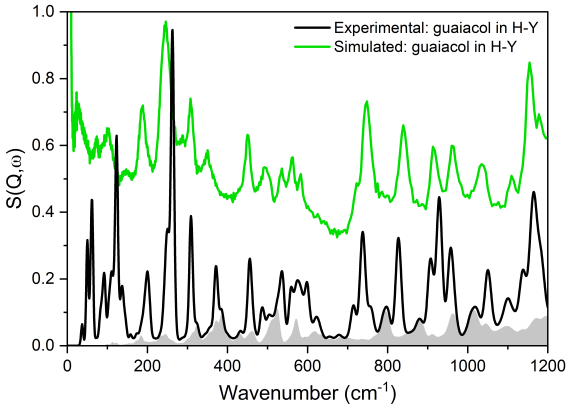

(a) Guaiacol in H-Y

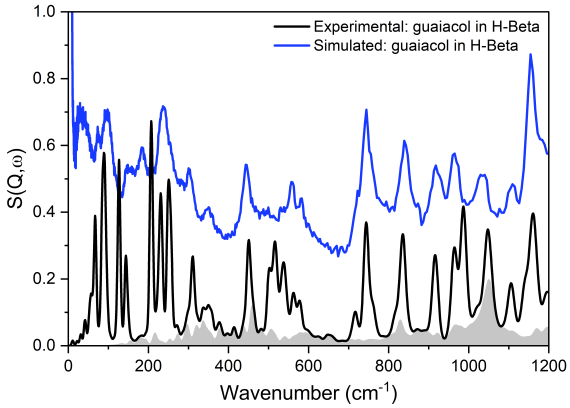

(b) Guaiacol in H-Beta

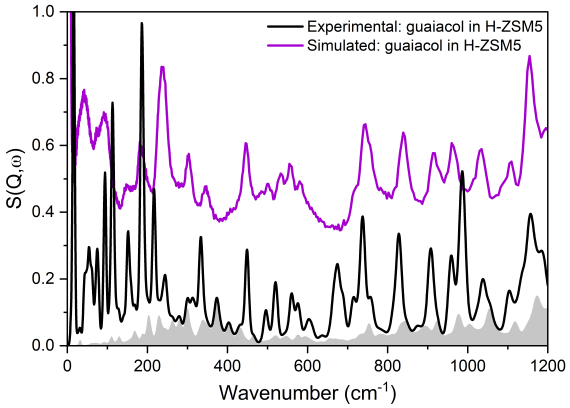

(c) Guaiacol in H-ZSM5

Figure S22: Comparisons of the simulated and experimental INS spectra used to identify modes related to each peak for guaiacol in each zeolite.

Table S8: Assignment of vibrational modes to peaks in the INS spectra of crystalline guaiacol and descriptions of the spectral changes upon its loading into zeolites.

Frequency (cm^{-1})	Vibrational modes	Significant spectral changes for the zeolite samples
148	Ome ring oop bend	decreased intensity
203	all oop bend, me rotation	red-shift, decreased intensity (H-Beta)
240	sym Ome, OH ip bend	–
252	all oop bend, me rotation	red-shift, decreased intensity, broader
315	sym all oop bend, me rotation	red-shift, decreased intensity
350	sym Ome, OH ip bend	decreased intensity
458	OH, ring oop bend	red-shift
498	all ip bend (identical O bend to anisole at 554)	decreased intensity
537	all ip bend	decreased intensity
564	ring (all) oop bend	–
582	all ip bend	–
725	ring oop bend	–
754	sym ring oop bend (and all ip stretch)	red-shift, broader
843	asym ring oop bend (and all ip stretch)	–
916	ring oop bend	–
961	ring oop bend	–
1035	Ome, ring ip stretch and ring ip bend	–
1110	Ome ip stretch, OH, ring ip bend	–
1155	ring ip bend	–

As with the other molecules when guaiacol is dosed into zeolites we observe many peak shifts to lower frequencies, especially for modes involving the hydroxyl group, alongside peaks that showed significant reductions in peak intensities, and peak broadenings, with greater changes observed going from H-Y to H-Beta to H-ZSM5. Also observed was the same decrease in intensity, from crystalline guaiacol to H-Y and completely disappearing in H-Beta and H-ZSM5 for the mode at 554 cm^{-1} in the experimental samples. Whilst this mode shows the ip bend of all the guaiacol hydrogen's, the dominating motion is the ip bend of the methoxy oxygen, equivalent to the motion at 554 cm^{-1} present in the anisole experimental spectra. However, due to greater uncertainties in most peak assignments of guaiacol, caused by unresolved peaks in the experiment and an absence of the simulated crystalline structure of guaiacol and weaker reproductions of the zeolite samples, we have not investigated most of these changes in detail, as with other systems in Section 3.2.

References

(1) N. T. Ramírez-Marquez, D. J. Pérez-Martínez and C.-A. Trujillo, *Microporous and Mesoporous Materials*, 2023, **360**, 112700.

(2) Z. S. Qureshi, T. Kella, R. Lawal, M. M. Hossain and S. A. Ali, *Chemical Engineering Research and Design*, 2025, **215**, 494–506.

(3) P. Losch, T. C. Hoff, J. F. Kolb, C. Bernardon, J.-P. Tessonnier and B. Louis, *Catalysts*, 2017, **7**, DOI: 10.3390/catal7080225.

(4) S. Li, Z. Zhao, R. Zhao, D. Zhou and W. Zhang, *ChemCatChem*, 2017, **9**, 1494–1502.

(5) A. Vjunov, J. L. Fulton, T. Huthwelker, S. Pin, D. Mei, G. K. Schenter, N. Govind, D. M. Camaioni, J. Z. Hu and J. A. Lercher, *Journal of the American Chemical Society*, 2014, **136**, 8296–8306.

(6) A. V. Vorontsov and P. G. Smirniotis, *The Journal of Physical Chemistry A*, 2022, **126**, 7840–7851.

(7) C. Li, X. Dong, H. Yu and Y. Yu, *Physical Chemistry Chemical Physics*, 2023, **25**, 24547–24562.

(8) C. Hernandez-Tamargo, A. O'Malley, I. P. Silverwood and N. H. de Leeuw, *Catalysis Science & Technology*, 2019, **9**, 6700–6713.

(9) R. Zhao, Z. Zhao, S. Li and W. Zhang, *The Journal of Physical Chemistry Letters*, 2017, **8**, 2323–2327.

(10) A. R. Ruiz-Salvador, R. Grau-Crespo, A. E. Gray and D. W. Lewis, *Journal of Solid State Chemistry*, 2013, **198**, 330–336.

(11) J. Holzinger, P. Beato, L. F. Lundegaard and J. Skibsted, *The Journal of Physical Chemistry C*, 2018, **122**, 15595–15613.

(12) S. M. Opalka and T. Zhu, *Microporous and Mesoporous Materials*, 2016, **222**, 256–270.

(13) A. T. Smith, P. N. Plessow and F. Studt, *The Journal of Physical Chemistry C*, 2021, **125**, 20373–20379.

(14) N. Zhang, C. Liu, J. Ma, R. Li and H. Jiao, *Physical Chemistry Chemical Physics*, 2019, **21**, 18758–18768.

(15) X. Tang, W. Chen, W. Dong, Z. Liu, J. Yuan, H. Xia, X. Yi and A. Zheng, *Catalysis Today*, 2022, **405-406**, 101–110.

(16) S. Wang, P. Wang, Z. Qin, Y. Chen, M. Dong, J. Li, K. Zhang, P. Liu, J. Wang and W. Fan, *ACS Catalysis*, 2018, **8**, 5485–5505.

(17) E. N. Domoroshchina, R. D. Svetogorov, G. M. Kuz'micheva, G. V. Kravchenko, L. V. Pirutko, A. I. Zhukova, A. N. Utenyshev and K. V. Bozhenko, *Journal of Materials Science*, 2023, **58**, 3934–3946.

(18) D. H. Olson, N. Khosrovani, A. W. Peters and B. H. Toby, *The Journal of Physical Chemistry B*, 2000, **104**, 4844–4848.

(19) E. Dib, T. Mineva, E. Veron, V. Sarou-Kanian, F. Fayon and B. Alonso, *The Journal of Physical Chemistry Letters*, 2017, **9**, 19–24.

(20) H. Jobic, *Microporous and Mesoporous Materials*, 2002, **55**, 159–169.

(21) W. Jacobs, H. Jobic, J. van Wolput and R. van Santen, *Zeolites*, 1992, **12**, 315–319.

(22) T. Lemishko, S. Valencia, F. Rey, M. Jiménez-Ruiz and G. Sastre, *The Journal of Physical Chemistry C*, 2016, **120**, 24904–24909.

(23) M. J. Wax, R. R. Cavanagh, J. J. Rush, G. D. Stucky, L. Abrams and D. R. Corbin, *The Journal of Physical Chemistry*, 1986, **90**, 532–534.

(24) J. Sauer, *Journal of Molecular Catalysis*, 1989, **54**, 312–323.

(25) N. Sivasankar and S. Vasudevan, *The Journal of Physical Chemistry B*, 2004, **108**, 11585–11590.

(26) G. Piccini, M. Alessio and J. Sauer, *Physical Chemistry Chemical Physics*, 2018, **20**, 19964–19970.

(27) Y. Zhang, J. Yu, Y.-H. Yeh, R. J. Gorte, S. Rangarajan and M. Mavrikakis, *The Journal of Physical Chemistry C*, 2015, **119**, 28970–28978.

(28) P. N. Plessow and F. Studt, *The Journal of Physical Chemistry Letters*, 2020, **11**, 4305–4310.

(29) M. Xing, Y. Chen, J. Cao, Y. Han, Z. Tao, F. Wang, K. Hao, L. Zhang, W. Zheng, H. Xiang, Y. Yang, Y. Li and X. Wen, *Fuel*, 2023, **333**, 126541.

(30) A. V. Vorontsov, P. G. Smirniotis and U. Kumar, *Catalysts*, 2023, **13**, 833.

(31) M. Fischer, F. O. Evers, F. Formalik and A. Olejniczak, *Theoretical Chemistry Accounts*, 2016, **135**, DOI: 10.1007/s00214-016-2014-6.

(32) V. V. Mihaleva, R. A. van Santen and A. P. J. Jansen, *The Journal of Physical Chemistry B*, 2001, **105**, 6874–6879.

(33) K. Stanciakova, J. N. Louwen, B. M. Weckhuysen, R. E. Bulo and F. Göltl, *The Journal of Physical Chemistry C*, 2021, **125**, 20261–20274.

(34) Y. Zhang and W. Yang, *Physical Review Letters*, 1998, **80**, 890–890.

(35) E. Batisai, V. J. Smith, S. A. Bourne and N. B. Báthori, *CrystEngComm*, 2015, **17**, 5134–5138.

(36) C. Bois, *Acta Crystallographica Section B Structural Crystallography and Crystal Chemistry*, 1970, **26**, 2086–2092.

(37) M. Perrin and A. Thozet, *Cryst. Struct. Commun.*, 1974, **3**, 661.

(38) I. J. Bruno, J. C. Cole, P. R. Edgington, M. Kessler, C. F. Macrae, P. McCabe, J. Pearson and R. Taylor, *Acta Crystallographica Section B Structural Science*, 2002, **58**, 389–397.

(39) C. Bois, *Acta Crystallographica Section B Structural Crystallography and Crystal Chemistry*, 1973, **29**, 1011–1017.

(40) I. D. H. Oswald and W. A. Crichton, *CrystEngComm*, 2009, **11**, 463–469.

(41) C. Bois, *Acta Crystallographica Section B Structural Crystallography and Crystal Chemistry*, 1972, **28**, 25–31.

(42) R. W. Seidel and R. Goddard, *Acta Crystallographica Section C Structural Chemistry*, 2015, **71**, 664–666.

(43) I. B. Adilina, N. Rinaldi, S. P. Simanungkalit, F. Aulia, F. Oemry, G. B. G. Stenning, I. P. Silverwood and S. F. Parker, *The Journal of Physical Chemistry C*, 2019, **123**, 21429–21439.

(44) T. Ebata, N. Mizuochi, T. Watanabe and N. Mikami, *The Journal of Physical Chemistry*, 1996, **100**, 546–550.